Resonance-Based Detection of Magnetic Nanoparticles and Microbeads Using Nanopatterned Ferromagnets

Manu Sushruth,[1] Junjia Ding,[2,*] Jeremy Duczynski,[3] Robert C. Woodward,[1] Ryan A. Begley,[1] Hans Fangohr,[4] Rebecca O. Fuller,[3] Adekunle O. Adeyeye,[2] Mikhail Kostylev,[1] and Peter J. Metaxas[1,†]

[1]*School of Physics, M013, University of Western Australia, 35 Stirling Highway, Crawley, Western Australia 6009, Australia*

[2]*Department of Electrical and Computer Engineering, National University of Singapore, 4 Engineering Drive 3, Singapore 117576, Singapore*

[3]*School of Chemistry and Biochemistry, M310, University of Western Australia, 35 Stirling Highway, Crawley, Western Australia 6009, Australia*

[4]*Faculty of Engineering and the Environment, University of Southampton, Southampton SO17 1BJ, United Kingdom*

(Received 28 June 2016; published 5 October 2016)

Biosensing with ferromagnet-based magnetoresistive devices has been dominated by electrical detection of particle-induced changes to a device's (quasi-)static magnetic configuration. There are however potential advantages to be gained from using field dependent, high frequency resonant magnetization dynamics for magnetic particle detection. Here, we demonstrate the use of nanoconfined ferromagnetic resonances in periodically nanopatterned magnetic films for the detection of adsorbed magnetic particles having diameters ranging from 6 nm to 4 μm. The nanopatterned films contain arrays of holes which appear to act as preferential adsorption sites for small particles. Hole-localized particles act in unison to shift the frequencies of the patterned layer's ferromagnetic-resonance modes, with shift polarities determined by the localization of each mode within the nanopattern's repeating unit cell. The same polarity shifts are observed for a large range of coverages, even when quasicontinuous particle sheets form above the hole-localized particles. For large particles, preferential adsorption no longer occurs, leading to resonance shifts with polarities that are independent of the mode localization, and amplitudes that are comparable to those seen in continuous layers. Indeed, for nanoparticles adsorbed onto a continuous layer, the particle-induced shift of the layer's fundamental mode is up to 10 times less than that observed for nanoconfined modes in the nanopatterned systems, the low shift being induced by relatively weak fields emanating beyond the particle in the direction of the static applied field. This result highlights the importance of having particles consistently positioned in the close vicinity of confined modes.

DOI: 10.1103/PhysRevApplied.6.044005

I. INTRODUCTION

Magnetic biosensing techniques have shown excellent promise in terms of providing a matrix-insensitive biological-detection platform for applications such as (point-of-care) medical diagnostics [1–3] and food-safety monitoring [4]. These techniques center on the detection of magnetic particles which are used as tags for analytes of interest in (biological) fluids [Fig. 1(a)]. Importantly, the absence of magnetic backgrounds in the majority of biological fluids enables magnetic biodetection in minimally processed or unprocessed samples (see, e.g., Refs. [5–7]). While numerous methods for the electronic detection of nanoparticles exist [3,8–18], giant or tunneling magnetoresistive magnetic-field sensors have garnered significant interest [1,2,6,19–23]. Conventional sensing approaches using such devices are typically based on the magnetoresistive detection of magnetic-particle-induced changes to the static magnetic configuration within the device [Fig. 1(b)] [24]. Thus, like Hall-effect sensors [14,15,25], these approaches offer a sensing method based on detecting changes to a (potentially modulated) dc voltage level.

However, it is also possible to exploit the magnetic-field dependence of resonant magnetization dynamics for particle sensing [26–31]. Indeed, the precession frequency of the magnetization (which is typically in the gigahertz range) will be altered by particle-generated magnetic fields due to an intrinsic magnetic-field-dependence of ferromagnetic-resonance (FMR) [Fig. 1(c)]. This approach opens the way for an intrinsically frequency-based, rather than amplitude-based, sensing technique [26,32]. One potential advantage of this technique is that the stray magnetic fields generated by the particles act directly on the precessing moments, avoiding magnetoresistive sensing's requirement of detecting particle-induced changes to the

*Present address: Argonne National Laboratory, 9700 South Cass Avenue, Argonne, IL 60439, USA.

†peter.metaxas@uwa.edu.au

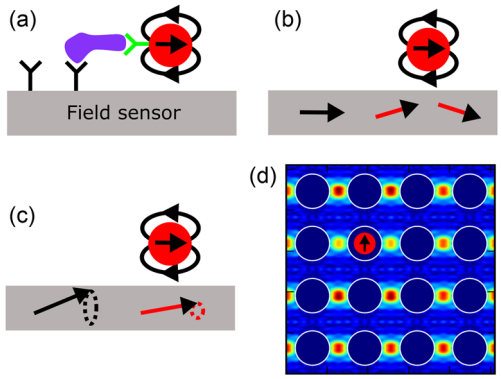

FIG. 1. (a) Schematic of a sandwich immunoassay showing a magnetically labeled biological entity specifically bound to a chemically functionalized magnetic-field sensor. The nanoparticle stray field can induce changes to the (b) static magnetization configuration of a ferromagnetic sensing element or (c) its precessional magnetization dynamics. (d) A spherical magnetic nanoparticle (red) within a hole (white circles) in a hole-based, periodic magnonic crystal with a geometry equivalent to that studied in Sec. II B (300-nm-wide holes). Both the particle and the patterned film are magnetized towards the top of the page. The particle stray field locally modifies the amplitude of precessional magnetization dynamics around it. The dynamics correspond to a side-mode resonance which is localized between the holes. The color encodes the amplitude of the magnetization precession in the magnetic layer (red, high; blue, low). Except for the single nanoparticle, there is no magnetic material within the holes.

magnetic configuration of the system [31]. As a result, resonance-based sensing can be carried out in the presence of large external fields where particle-generated fields are maximized (i.e., sensing can be realized even when the sensor's magnetic state is saturated and is therefore insensitive to small changes in the local field) [31,33]. Furthermore, the use of spin-torque oscillators [26,32] enables electrical readout of magnetization dynamics in real time [34–37], potentially enabling high-speed sensing with sub-100-nm devices [26] for applications such as cytometry [25,38–40]. Note that one of the FMR modes used here for particle detection is confined laterally to a region with a size on the order of 100×100 nm^2.

This work focuses on magnonic crystals (MCs), which are attractive systems for exploring the fundamentals of a resonance-based sensing technique for magnetic (nano) particles. MCs are magnetic materials which have been artificially patterned (typically at the nanoscale) to control spin-wave (magnon) propagation or enable periodic confinement of nanolocalized ferromagnetic resonances [41] [see, e.g., Fig. 1(d)]. High levels of periodicity over large length scales mean that these systems' nanolocalized FMR modes (analogous to those excited in isolated nanostructures) can be probed easily in laboratory settings in macroscopic samples (see, e.g., Ref. [42]). Beyond envisioned applications in data and signal processing (see, e.g., Ref. [43]), we previously demonstrated that MCs can be used to understand the influence of magnetic fields generated by magnetic nanoparticles on highly localized ("spatially confined") ferromagnetic resonances [30]. Notably, using a hole-based structure enables the localization of particles within the holes, with a subsequent predictable local modification of the resonant precession of the magnetization in the neighborhood of the captured particle. An example of this modification can be seen in Fig. 1(d) as a change in the color-coded precession amplitude to the left and right of the hole-localized nanoparticle. More recently, similar effects were confirmed numerically in another hole-based MC geometry [44].

In this paper, we demonstrate the use of nanolocalized ferromagnetic-resonance modes for the detection of magnetic particles with a range of diameters spanning 3 orders of magnitude: from sub-10-nm superparamagnetic iron-oxide nanoparticles to 4-μm-wide beads. This particle-size range also approximates a correspondingly large range of biological length scales, from single proteins [45,46] to exosomes [47] and cells [18,25]. In this paper, we explicitly show the advantage of using hole-based structures for the localization of both modes and particles, the latter ensuring a common, and thus reinforcing effect from individual nanoparticles. Indeed, we show that the sensitivity can be an order of magnitude less when using an unpatterned (i.e., continuous) ferromagnetic layer. There, the dominant effect is from the stray magnetic field extending relatively far beyond the particle radius, which is weak compared to that beneath or directly neighboring each particle. For nanoparticles within a nanopatterned MC's holes, however, the localization of different FMR modes in the regions directly surrounding each hole can lead to large shifts of the modes' frequencies, with the mode localization defining the sign of the frequency shift. Notably, this shift polarity is maintained and its amplitude increased at high particle coverages where quasicontinuous sheets of particles form. However, by increasing the particle size to a degree in which the particle cannot enter the holes, we lose the mode-dependent shift polarities with all modes behaving similarly to the fundamental mode of a continuous layer in that their frequencies all increase. Varying the particle size can thus enable a transition to filmlike sensing behavior, albeit with multiple modes existing in the patterned MC. Note that all particles studied in this work exhibit a quasinull magnetic moment in zero field (as checked via magnetometry), and thus minimal agglomeration.

II. METHODS

A. Experimental details

The nanopatterned films studied here consist of square arrays of circular holes ("antidots") in a 30-nm-thick Permalloy ($Ni_{80}Fe_{20}$) film with a 5- or 10-nm gold (Au) capping layer. The array pitch is 450 nm, with hole diameters of 240 or 300 nm. The large area (4×4 mm^2)

MCs are fabricated on silicon (Si) substrates using deep-ultraviolet lithography, e-beam deposition and lift-off [48]. The continuous layer studied in Sec. III A has the same composition as the MCs.

FMR measurements of the continuous films and nanopatterned MCs are obtained using broadband microwave stripline-based FMR spectroscopy (see, e.g., Ref. [49]), a technique where resonant magnetization dynamics are excited in magnetic materials using a radio-frequency (rf) field, here generated by a rf signal passing through an underlying stripline. An absorption of microwave power by the magnetic sample is measured when the frequency of the rf field matches that of a FMR mode. Here, we use field-modulated FMR spectroscopy wherein a lock-in amplifier measures the external field (H_{ext}) derivative of the FMR response at a constant frequency while sweeping H_{ext} using an electromagnet. An interferometric receiver is used to maximize signal amplitudes [50]. This choice is particularly important in our measurement since the sample is separated from the stripline by a microscope coverslip (rather than sitting directly on the stripline). The coverslip ensures that particles do not rub off onto the microstripline but reduces the signal amplitude. H_{ext} is measured with a teslameter (FH 54; Magnet-Physik Dr. Steingroever GmbH) and typically swept between approximately 0 and 350 mT. We note that an overall decrease in the differential FMR signal is seen when adding increasing concentrations of particles. To enable a comparison of traces, the traces are vertically scaled. A small vertical offset (a few tens of microvolts, at most) also had to be corrected for in some cases.

Particle detection is carried out for a range of particles with average or supplier-stated diameters of 6, 50, 130, and 880 nm and 4.14 μm (see the Appendix for further details). Particles are applied in solution to the upper surface of the film or MC in ambient laboratory conditions outside of the measurement setup in the absence of an external magnetic field ($H_{\text{ext}} = 0$). The solutions are then allowed to dry before (a) imaging the particle-covered film or MC via scanning-electron microscopy and (b) remeasuring the FMR traces. For each frequency and particle coverage, at least three FMR spectra are obtained. Before each spectrum measurement, the sample is again physically removed from the setup and replaced. This enables a determination of the uncertainty in the resonance field measurement that is associated with the sample removal and replacement step which occurs during particle application. This uncertainty is typically on the order of 0.5 mT or less.

B. Micromagnetic simulations

Micromagnetic simulations are carried out to predict field-dependent FMR-mode frequencies and spatial profiles of the FMR modes. They are run for a single unit cell (450×450 nm^2) of the MC's hole array or an equivalently sized region of continuous film. We employ periodic boundary conditions and a tiled macrogeometry [51] (33×33 unit cells). The following parameters are used for the patterned MC and the unpatterned films: damping $\alpha = 0.008$, no intrinsic anisotropy, gyromagnetic ratio $2\pi\gamma = 1.85 \times 10^{11}$ rad/Ts, saturation magnetization $M_S = 8 \times 10^5$ A/m, and exchange stiffness $A_{\text{ex}} = 13$ pJ/m.

Micromagnetic simulations are used to determine the effect of the 130-nm-wide nanoparticles on the FMR modes. For such simulations, the simulation region is extended vertically to enable us to explicitly include discretized spherical nanoparticles within the simulation's macrogeometry. Note that, although the supplier-provided nanoparticle size is 130 nm, we use a width of 150 nm in the simulations, as in Ref. [30]. For nanoparticles lying within the holes of the patterned layer, the lower surface of the spherical particle is always aligned with the lower surface of the magnetic layer (i.e., resting on the underlying Si wafer). For particles on top of the ferromagnetic layer's surface, the lower surface of the particle is set at 10 nm above the upper surface of the magnetic layer (i.e., sitting on the upper surface of the nonmagnetic capping layer). For the simulation, nanoparticles are treated as ferromagnets with damping $\alpha = 0.05$, gyromagnetic ratio γ as above, and an H_{ext}-dependent M_S taken from magnetometry measurements of freeze-dried nanoparticles [30].

MuMax3 [52] is used to obtain the presented micromagnetic-simulation results. The system is first initialized with a uniform magnetization in the (0.5, 1) direction and allowed to relax in the presence of an external field (applied along the y axis) using MuMax3's internal-relaxation routine. Following the relaxation stage, an excitation sinc pulse of 0.5 mT (cutoff frequency, 30 GHz; 300-ps offset) is applied along the x axis to induce resonant precessional magnetization dynamics. The resultant damped ringdown of the spatially averaged x component of the magnetization, m_x (recorded in the time domain), is then Fourier analyzed to the extract the resonant frequencies. All resultant mode-profile visualizations are determined by extracting the spatially resolved m_x Fourier amplitudes at each identified resonant frequency across the simulation region. The obtained results are shown as intensity plots, with the brightest regions corresponding to the highest Fourier amplitudes for m_x at that frequency [see, for example, the Fig. 2(a) insets]. The Matplotlib, NumPy, and SciPy [53,54] packages are used for analysis and visualization of the simulation data. The eigensolver (see, e.g., Refs. [31,55]) in the FinMag micromagnetic-simulation package (based on Nmag [56]) is also used for some test cases, with good levels of agreement [30] (see, e.g., Fig. 1 in the Supplemental Material [57]).

III. RESULTS AND DISCUSSION

A. Continuous layers

We first consider the case of particle-induced shifts of the fundamental FMR mode in continuous, *unpatterned*

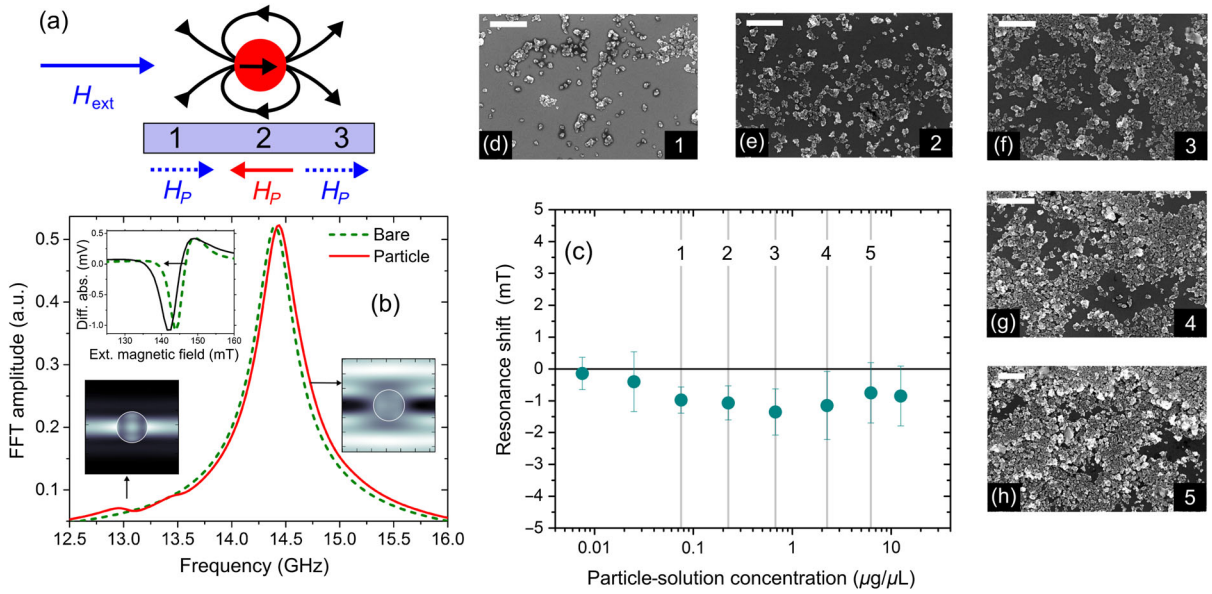

FIG. 2. (a) Schematic side view of a magnetic nanoparticle above a continuous magnetic film. The in-plane stray magnetic field generated by the particle, H_P, is strong and opposes the applied in-plane static field (H_{ext}) directly below it, resulting in a large downward shift in the resonance frequency in that region (marked with a 2). In regions 1 and 3, H_P is weaker (the blue dashed lines) but reinforces H_{ext}, thus slightly increasing the resonance frequency. (b) Fourier-transformed time-domain simulation data for an unpatterned film showing a small upward shift in the fundamental mode's frequency in the presence of a particle. The upper-left inset shows (scaled) experimental FMR traces, obtained at 12 GHz, with (solid black line) and without (dotted green line) particles on the unpatterned film's surface (the concentration is 0.675 $\mu g\,\mu L^{-1}$). The lower insets show the simulated mode profiles of the two main modes that exist in the presence of a particle. In these simulations, the field is oriented towards the top of the page. (c) Experimentally obtained fundamental mode shifts in an unpatterned film as a function of particle solution concentration. The presented values are the averages of the shifts obtained at different rf frequencies (11.5–16 GHz) with the error bars showing the spread in the measured values as well as the uncertainty related to slight variations in sample placement. (d)–(h) SEM images showing the distribution of particles on the unpatterned film's upper surface at the particle concentrations labeled as 1–5 in (c). White scale bars are 1 μm long.

magnetic layers where, in the absence of particles, resonant dynamics are typically laterally uniform across the layer. Figure 2(a) shows a schematic of the dipole field of a magnetic particle acting on an underlying magnetic film subject to an external in-plane static field, H_{ext}. The in-plane component of the particle's field, H_P, is strong and opposes H_{ext} directly below the particle [in region 2, Fig. 2(a)] and to the sides of the particle, the latter due to the symmetry of the dipolar H_P. Elsewhere [regions 1 and 3, Fig. 2(a)], the in-plane component of H_P is weaker but reinforces H_{ext}. Subsequently, although a bare, thin magnetic layer has one primary resonance mode [which corresponds to the spatially uniform fundamental mode, shown as a dashed line in Fig. 2(b)], an additional, low-frequency mode appears in simulation when isolated particles are on top of the film [solid line in Fig. 2(b)].

The low-frequency mode is located beneath the particle and to its sides, where H_P opposes H_{ext} [see the bottom-left inset in Fig. 2(b) while making a comparison to region 2 in Fig. 2(a)]. Since the total field is reduced at that position, so is the resonance frequency. The majority of the dynamics within the layer are, however, concentrated in the remainder of the simulation region, as seen in the bottom-right inset of Fig. 2(b) [these areas correspond to regions 1 and 3 in Fig. 2(a)]. This mode is slightly upshifted in frequency [Fig. 2(b)] due to the weak H_P in those regions reinforcing H_{ext}, which increases the total field acting on the precessing moments. Notably, at a particle-layer separation of 10 nm, the maximum in-plane H_P directly below a single, perfectly spherical particle will be approximately 15 times higher than the maximum in-plane H_P at the upper and lower boundaries of the computation cell. This effect explains the disparity in the shift amplitudes seen for the dynamics concentrated in region 2 versus those concentrated in regions 1 and 3.

In a field-resolved experimental FMR trace [obtained at a fixed frequency; see the upper-left inset of Fig. 2(b) for an example], the predicted particle-induced frequency upshift of the fundamental mode manifests as a downshifted resonance field. This resonance field shift is due to the reinforcing effect of H_p, which reduces the magnitude of the external field that must be applied to meet the resonance condition. In Fig. 2(c), we show the consistently negative experimentally observed shift of the fundamental resonance for increasing particle coverages. Different particle coverages are obtained by applying consecutively higher concentrations of particle-containing solutions to the film and measuring

the FMR spectra between each application. Note that the shift is highest for intermediate particle coverages [Figs. 2(f) and 2(g)], where there are large numbers of isolated particles or clusters of particles on top of the layer. As expected, low particle coverages [Figs. 2(d) and 2(e)] lead to a low reinforcing H_P when averaged across the film, and thus a low measured resonance field shift. At high coverages, however, quasicontinuous particle layers form which also generate relatively small shifts. These shifts are likely small because the particle sheets approximate continuous layers which, ignoring effects of roughness and lateral boundaries, generate negligible stray fields.

The average resonance-frequency shift obtained from the simulation (Sec. II B) is 34 MHz ($\equiv$0.7 mT, given an experimentally measured slope of 49.4 GHz/T for the fundamental mode; see Fig. 2 in the Supplemental Material [57]). This result is comparable to the maximum experimentally observed field shift in the continuous layer (1.3 ± 0.7 mT). Thus, we can conclude that the weak shift observed for the continuous layer is not a result of an intrinsically low field sensitivity of the resonance. In fact, it is actually quite high, at almost 50 GHz/T. Rather, the weak shift is due to the dominant FMR signal coming from portions of the film subject to the relatively weak reinforcing H_P fields that surround the particles laterally [i.e., regions 1 and 3 in Fig. 2(a)] instead of the more intense H_P fields located directly beneath the particles.

B. Patterned films: Hole arrays

We now turn to the nanopatterned MCs for which it is possible to have spatially localized resonances in regions where H_P is large. The main panel in Fig. 3(a) shows a simulated ferromagnetic resonance spectrum at $H_{\text{ext}} =$ 180 mT for a MC with 300-nm-wide holes on a 450-nm square lattice. The excitation spectrum is clearly much richer than the continuous layer with a number of resonant modes, each having different localizations within the unit cell [Fig. 3(b)]. The simulated traces have been differentiated with respect to frequency for a more natural comparison to the experimental FMR traces. We focus predominantly on the side mode [SM; shown also in Fig. 1(d)] and the extended mode (EM) with the intermediate modes (IMs) and edge mode (EdM) discussed only briefly. While the SM is largely localized between horizontally neighboring holes, the EM occurs over extended bands running between rows of holes orthogonal to the applied field [Fig. 3(b)]. IM1–IM3 have similar localizations to that of the EM. Good agreement is found between the simulation and the experiment for both the overall mode spectrum and the frequencies of the EM and the SM (see Fig. 3 in the Supplemental Material [57]).

Depending on the spatial localization of each mode, the stray magnetic field from magnetized particles within the holes has a y component which can locally reinforce or oppose the y-oriented external field [30,58]. This result is shown schematically for the SM and the EM in Fig. 3(b) (one can consider the more localized modes as being nanoscale dynamic probes for the particle stray fields). Since the y component of H_P opposes H_{ext} where the SM is localized, the mode's frequency reduces due to a reduced net field at that location. This reduction is seen in Fig. 3(a), where we have also included the resonance spectrum that has been simulated in the presence of a 150-nm-wide particle at the lateral center of the simulation region's antidot. In contrast, the EM (and EdM) resonances shift upwards in frequency since H_P reinforces H_{ext} at the upper and lower parts of the unit cell. Note that the confinement of the modes in well-defined regions close to the particle where the stray fields are strong [i.e., directly to the sides of the particle ($\pm x$) and directly "in front of" or "behind it" ($\pm y$)] results in significant shifts being induced for both the EM and the SM (approximately 0.1–0.3 GHz: approximately 10 times larger than that observed for the continuous layer). This larger shift occurs despite the sensitivities of the MC's EM and SM to static, uniform external fields

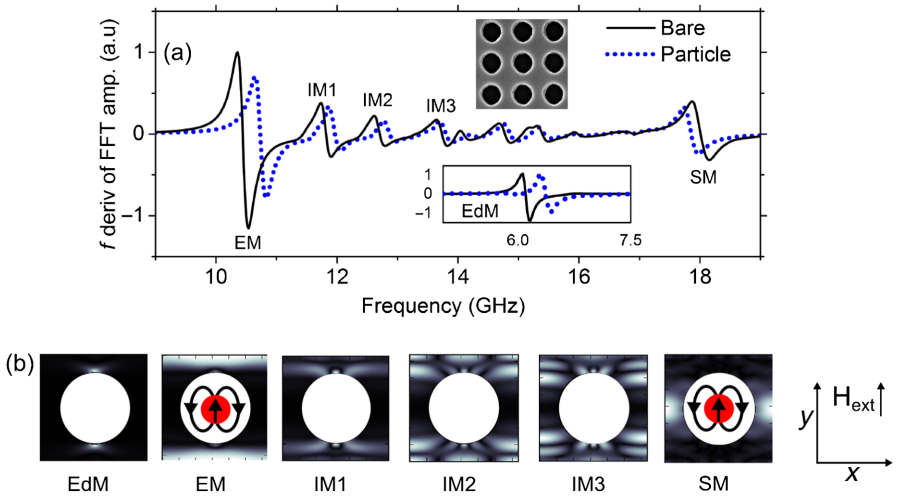

FIG. 3. (a) Simulated frequency resolved FMR spectra obtained at $\mu_0 H_{\text{ext}} =$ 180 mT applied in the y direction [see (b)] for a 300-nm MC with (dotted blue lines) and without (solid black line) a 150 nm wide particle within each hole. The upper inset shows a SEM image (1.3×1.3 μm) of the MC, and the lower inset shows the simulated resonance shift of the EdM in the presence of a particle. (b) Spatial concentration of dynamics for a number of resonance modes within a unit cell of the MC. A schematic of a particle and its stray field has been added to the EM and SM profiles.

being comparable to that of the continuous layer's fundamental mode. The EdM and IMs also display clear positive shifts in the presence of a hole-localized particle [Fig. 3(a)], consistent with the fact that they, like the EM, have their dynamics concentrated in the upper and lower portions of the unit cell (i.e., also subject to $H_P > 0$).

Following the same protocol as for the continuous layer in the previous section, we measured the SM and EM shifts versus particle concentration experimentally in a 300-nm MC (i.e., an MC with 300-nm-wide holes). The EM resonance field decreases since H_P locally increases the magnetic field [Fig. 4(a)]. The consequence of this decrease is that the resonance can be attained experimentally at a lower H_{ext} at each microwave frequency. The resonance fields of IM1–IM3, which have an EM-like localization, also shift downward experimentally (see Fig. 4 in the Supplemental Material [57]). In contrast, the SM resonance field increases because H_P locally shields the SM from H_{ext} [Fig. 4(b)]. This results in a larger H_{ext} having to be applied to attain the resonance condition. These shift directions are consistent with those seen in the frequency-resolved simulation data [Fig. 3(a)]. Quantitative comparisons of the measured and simulated shifts are made below.

As seen previously for low coverages [30], we observe a continuing increase of the shift magnitudes, with particle coverage over a very wide range of coverages [Fig. 4(c)]. For lower nanoparticle-solution concentrations, the majority of the particles are found within the holes [Figs. 4(d) and 4(e)], with both the percentage of filled holes and the percentage of particles lying within the holes increasing with the concentration of the applied particle solution (see Fig. 5 in the Supplemental Material [57]). Saturation of the shifts commences at the penultimate concentration, where a quasicontinuous layer of particles forms [Fig. 4(h)]. Notably, the maximum shifts in the MC are, as expected from the simulation, significantly higher (up to 10 times) than the maximum shift observed in the continuous layer. Note that the continuous-layer data from Fig. 2(c) has been plotted with the MC data in Fig. 4(c) to enable a direct comparison. Note also that while the continuous-layer resonance-field shifts decrease when a quasicontinuous particle sheet forms, in the MC sheet formation increases the observed shifts, an effect which is reproduced below via simulation.

We now discuss the reproduction of the observed shifts for the EM and the SM [Fig. 4(c)] at the two coverages which can be most easily simulated. The first coverage is

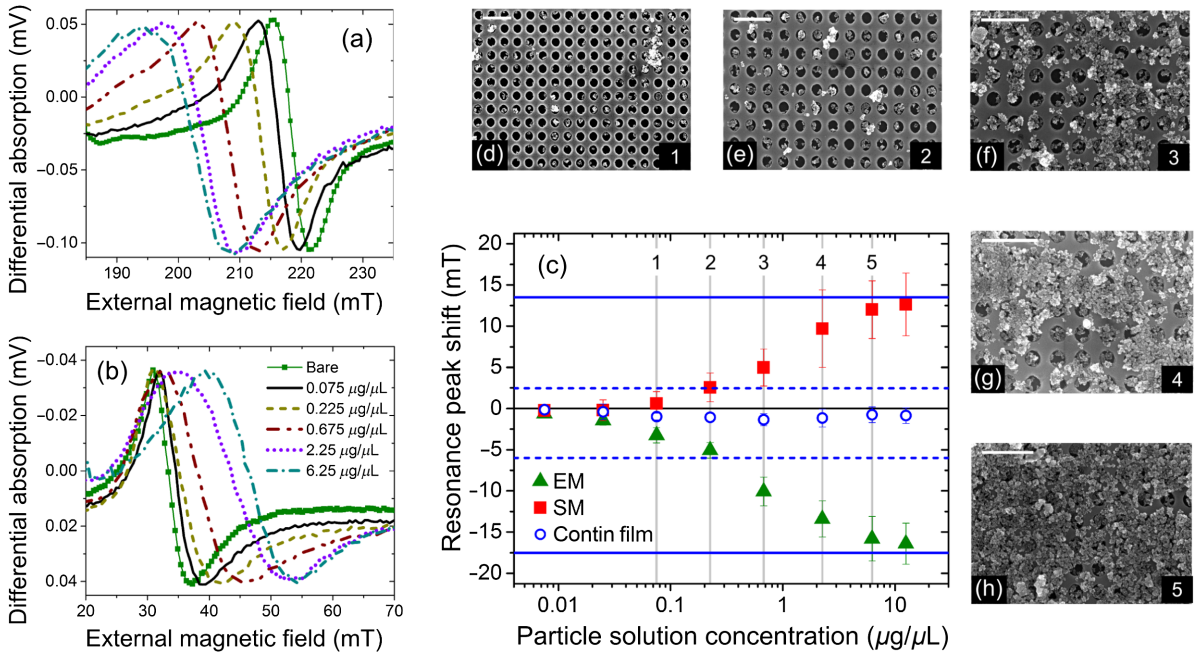

FIG. 4. (Scaled) experimental FMR traces (obtained at 12 GHz) showing shifts in the (a) EM and (b) SM resonances for increasing particle concentration. (c) The experimentally obtained EM and SM shifts for a 300-nm MC as a function of particle concentration. Horizontal dashed and solid lines show the simulated EM and SM shifts, respectively, for one particle per hole and the "disk + layer" geometry (the latter is discussed in the main text and is designed to replicate the effect of hole filling and continuous sheet formation). The error bars are a measure of the spread of shifts across the measured frequency range (11.5–16 GHz) and also include the uncertainties related to slight variations in sample placement. The continuous film's fundamental mode shift versus particle concentration [Fig. 2(c)] is also plotted (blue open circles) for a direct comparison with the patterned film. (d)–(h) SEM images showing cluster-shaped nanoparticles inside holes and on the upper surface of the MC at the particle concentrations labeled as 1–5 in (c). White scale bars are 1 μm long. The first four data points for the EM and the SM in (c) as well as the bare and two-lowest concentration traces in (a) were presented previously [30].

that obtained for 0.225 $\mu g/\mu L$, where there is approximately one particle in each hole [Fig. 4(e)]. There, simulations are carried out by adding a 150-nm-wide particle to the simulation at the hole center (as already described in Sec. II B) and observing the resultant shifts in the FMR-mode frequencies. For the high-coverage scenario, we replaced the particle with a disk (having a diameter 40 nm less than the hole diameter) which is covered by a contiguous 150-nm-thick continuous layer. This "disk + layer" had the same magnetic properties as the spherical particles (Sec. II B). It successfully approximated the high-particle-coverage scenario [Figs. 4(g) and 4(h)], where the filled holes are covered by a semicomplete particle sheet. The simulated shifts, converted from frequency shifts to field shifts using the data from Fig. 3(a) in the Supplemental Material [57], are shown in Fig. 4(c). There, we show the simulated shifts for the EM and the SM for one particle per hole (the horizontal dashed line) and full particle coverage (the solid dashed line). There is excellent agreement between these values and the shifts experimentally obtained, respectively, at the fourth and final coverages.

The simulated and experimental FMR resonance-field shifts given above are the averages of the shifts obtained at the different rf frequencies used in the experiment (11.5–16 GHz). When we change the rf frequency, however, we change the resonance field for each mode [as per Fig. 3(a) in the Supplemental Material [57]], and this change enables a measurement of the field dependence of the nanoparticle-induced FMR resonance-field shift. At low H_{ext}, the magnetization of the particles is reduced which subsequently reduces the shift observed for the SM (note that only the SM can be measured at low field for our frequency range). This reduced shift is shown in Fig. 5 with good agreement between the simulation and the experiment: experimental data has been obtained at 0.225 $\mu g/\mu L$, with

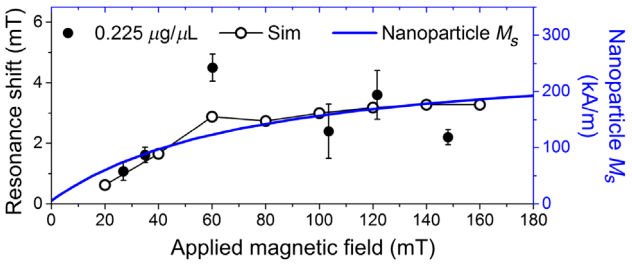

FIG. 5. (Left axis) Resonance-field shift versus external applied field for the SM in the 300-nm MC at 0.225 $\mu g/\mu L$, together with simulated SM-mode shifts for the case of one particle per hole. The simulated frequency shifts obtained are converted to fields using the data from Fig. 3(a) in the Supplemental Material [57]. Error bars on the experimental data points are due to uncertainties in sample placement. (Right axis) 130-nm-particle magnetization per unit volume at 300 K (measured using superconducting quantum-interference device magnetometry; the data were previously published in Ref. [30]).

the simulated shifts obtained under the assumption of one nanoparticle per hole (as above). Note that the simulations take into account the field-dependent moment of the particle which is also given in Fig. 5. The resonance-field shift is found to follow the H_{ext}-dependent-particle moment quite closely, approaching saturation at high field. This result highlights the ability to carry out resonance-based sensing even at high fields [31], where nanoparticle moments can be maximized. Field-dependent experimental resonance-field shifts for the SM and the EM at all coverages (up to $\mu_0 H_{ext} = 320$ mT for the EM), together with simulation results, are shown in Fig. 6 in the Supplemental Material [57].

We also demonstrate the ability to carry out particle sensing with a second MC having smaller holes (240 nm), but the same lattice pitch as the 300 nm MC. Analogous effects are observed, except that the shifts are reduced. The shifts can, albeit, be reproduced by assuming a filling proportional to the hole size (see Fig. 7 in the Supplemental Material [57]). This scenario is consistent with the reduced shifts having resulted from a reduced capability of filling rather than an intrinsically lower field sensitivity of the modes. Indeed, the intrinsic field sensitivities are comparable to those for the MC with 300-nm holes [see Figs. 3(a) and 3(c) in the Supplemental Material [57]].

C. The role of particle size and localization

In Figs. 6(a)–6(d), we show shifts in the EM resonance field induced by particles with different diameters: 6 nm, 50 nm, 0.88 μm, and 4.14 μm. Clear shifts are observed in all cases, demonstrating the compatibility of this sensing method with a very large range of particle sizes. As explained below, however, the polarities of the observed shifts depends on the size of the particles relative to the size of the holes. Before concentrating on the shift polarities, we briefly note that, as seen in Figs. 4(a) and 4(b) and Figs. 6(a)–6(d), the dominant effect of both nanoparticles and beads is typically a resonance shift, albeit accompanied by a relatively weak degree of linewidth broadening. Exceptions are the 0.88-μm particles and the highest-coverage scenario for the 6-nm particles, where broadening and shifts are comparable.

Opposing SM and EM shift polarities [as already seen in Fig. 4(c) for the 130-nm particles] are also observed for two other particle types, with the common aspect of these particles being that they can enter the MC's holes due to their small size: 6-nm-wide particles [see Fig. 6(a) and Fig. 8 in the Supplemental Material [57]] and 50-nm-wide particles [Figs. 6(b) and 6(e)–6(g)]. In both cases, the overall trend, as with the 130-nm particles, is a stronger shift with increasing particle coverage. This trend is seen clearly in Figs. 6(a) and 6(b), which show consecutively larger shifts of the EM resonance for both particle sizes. Note that a clear SM shift is seen for the 6-nm particles only at the highest concentration (see Fig. 8 in the Supplemental Material [57]).

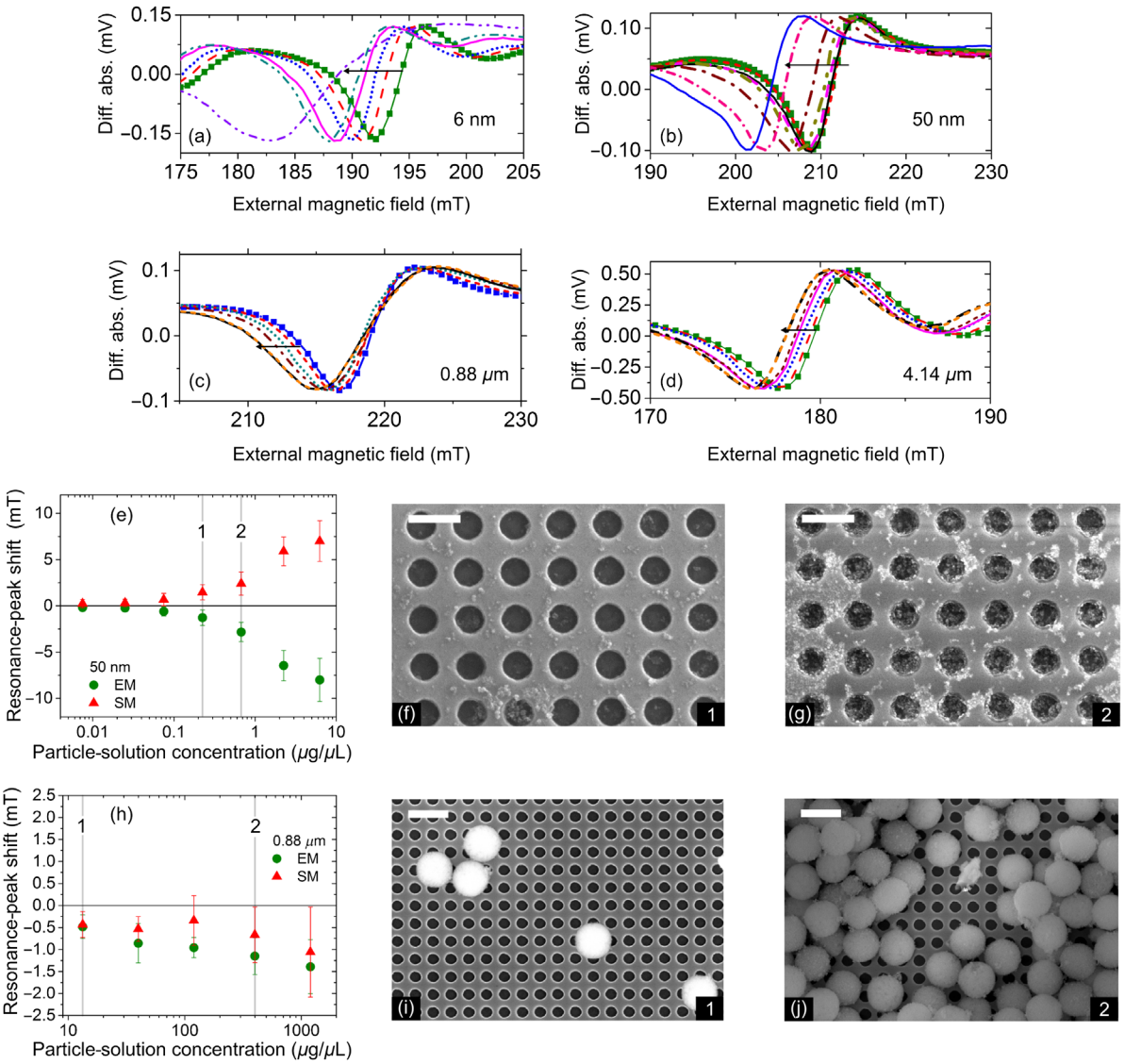

FIG. 6. (Scaled) experimentally obtained EM FMR traces obtained at 12 GHz showing a decrease in resonance field with an increase in concentration of (a) 6-nm nanoparticles, (b) 50-nm nanoparticles, (c) 0.88-μm magnetic beads, and (d) 4.14-μm magnetic beads. (e) EM and SM shifts as a function of applied 50-nm-particle concentrations. (f,g) SEM images showing the distribution of 50-nm particles at the particle concentrations labeled as 1 and 2 in (e). (h) EM and SM shifts as a function of applied 0.88-μm-bead concentrations. (i,j) SEM images showing the distribution of 0.88-μm-wide magnetic beads at the particle concentrations labeled as 1 and 2 in (h). The error bars in (e) and (h) are a measure of the spread of shifts across the measured frequency range (11.5–16 GHz) and include the uncertainty related to slight variations in sample placement. The white scale bars are 1 μm long.

For particles with diameters that are larger than the hole diameter however, both the SM and the EM are characterized by negative-polarity field shifts. The relevant data is shown in Figs. 6(c) and 6(h)–6(j) (0.88-μm beads) and Fig. 6(d) (4.14-μm beads; see also Fig. 8 in the Supplemental Material [57]). This behavior mirrors that observed for the fundamental FMR mode in the continuous, unpatterned layer in the presence of 130-nm-wide nanoparticles. This result suggests that, for large particles which are not predominantly hole localized, the dominant shift, as for the continuous layer, comes from in-plane fields which are generated by surface-located beads and which reinforce H_{ext}. Note that, although there is some centering of the 0.88-μm particles on top of holes observed at low concentrations [the two bottom-right particles in Fig. 6(i)], the larger particles are typically randomly distributed across the MC. As a result, for purely-surface-located beads, both the EM and the SM shift in the same direction since, when taking a macroscopic average over the sample, both of the modes are subject to equivalent parts of the particle-generated field profiles.

However, even with the *nanoparticles*, significant numbers of isolated particles or groups of particles also can be surface located. This observation has already been

highlighted for the 130-nm particles (Fig. 4) and can be seen clearly in Fig. 6(g) for the 50-nm particles. The shifts induced by isolated surface-located nanoparticles have been calculated via simulation for three different surface positions [scenarios II–IV in Fig. 7(a)] where simulated shifts of the SM and EM due to surface-located particles are compared to the shifts induced by a hole-located particles [scenario I in Fig. 7(a)]. The shifts, measured relative to the FMR frequency for a bare MC, are given in Figs. 7(b) and 7(c).

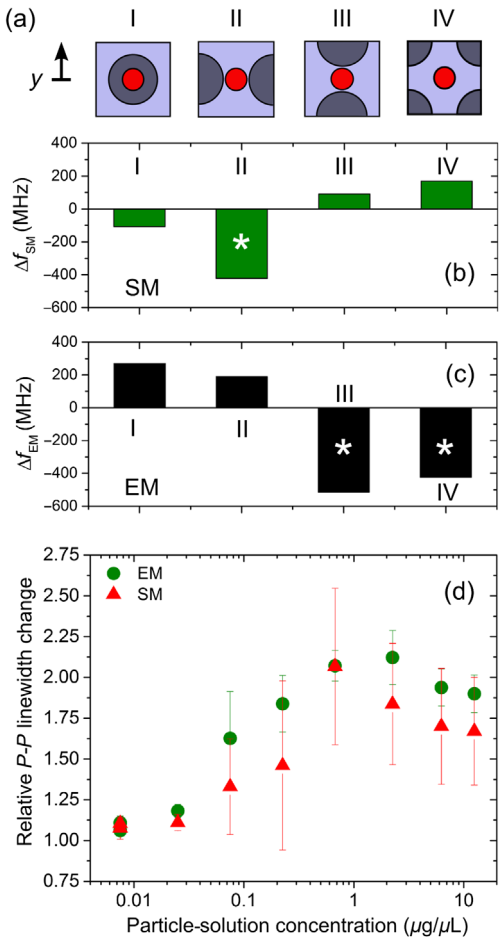

FIG. 7. (a) Schematics showing the particle positions with respect to the MC hole for scenarios I-IV, described below. Simulated (b) SM and (c) EM frequency shifts measured with respect to the bare frequency for a 150-nm particle located within the MC hole (I) and at various positions on the MC surface (II, above the SM region; III and IV, above the EM region). Large reductions in a mode's frequency (marked with an asterisk) are observed when a particle is above the region of the MC containing that mode. (d) Experimentally observed changes in the EM and SM resonance linewidths as a function of 130-nm-particle concentrations applied to the 300-nm MC. The error bars are a measure of the spread of linewidth broadening across the measured frequency range (11.5–16 GHz) and include uncertainties associated with sample replacement. Data for the lowest four concentrations are taken from Ref. [30].

When a particle is directly above the position where a mode's dynamics are concentrated, it can generate a resonance shift which is larger than that observed for hole-localized nanoparticles. Indeed, because of the geometrical confinement of FMR modes in the MC, the whole region containing the mode can be subject to the strong H_P which exists below a particle. This field opposes H_{ext} and is thus capable of strongly decreasing the resonance frequency of that mode. These strong reductions in the frequency are marked with asterisks in Figs. 7(b) and 7(c). They occur for the SM in scenario II, where the particle lies directly above the region where the SM is localized, and for the EM in scenarios III and IV, where the particle lies at points that are directly above the EM excitation band. When the EM or SM resonance frequency is strongly downshifted, the other mode experiences a weaker upshift since the other mode's dynamics will be located at a region where H_P is weak but reinforces H_{ext}, thus increasing the FMR frequency [equivalent to regions 1 and 3 in Fig. 2(a)]. The critical point here, though, is that the placement of small particles on the MC's upper surface is quite random within the unit cell. As a result, and as observed in the experiments on the 130 nm nanoparticles, the resonance shifts observed for the macroscopic MC are dominated by those induced by the hole-localized particles, even though the shifts induced locally by individual surface-located particles can be high with position-dependent polarities.

As already discussed (Sec. III B), in the experiments carried out with 130-nm particles, the majority of the particles are hole localized at low coverages and thus it is those particles which have a dominant effect on the modes (i.e., frequency downshifting for the SM and upshifting for the EM). At the other extreme (i.e., for high coverages), sheets form and, as already shown, the change is such that it reinforces the effect of hole-localized nanoparticles [Fig. 4(c)]. At intermediate coverages, however, there is a large number of isolated particles (or small groups of particles) on the MC's upper surface [e.g., the fifth-highest concentration; see Fig. 4(f)] and it is at this point that we observed a maximum in the linewidth broadening—the linewidth has been plotted versus particle concentration in Fig. 7(d). We propose that the large quantity of surface-located particles at these concentrations broadens the resonance linewidth by generating localized upshifting and downshifting across the macroscopic MC. The formation of a quasicontinuous layer of particles at higher coverages, however, would be expected to reduce the strong localized fields generated underneath the particles. Indeed, at these higher coverages, there is a slight reduction of the linewidth [Fig. 7(d)], consistent with a reduced contribution from isolated surface-located particles. We also note that distributions in the particle sizes [as can be identified in Figs. 4(d)–4(h)] will contribute to linewidth broadening since smaller (larger) particles will generate

smaller (larger) shifts (see Fig. 9 in the Supplemental Material [57]). This broadening will be unidirectional for a given mode, however, since both smaller and larger hole-localized particles generate shifts of the same polarity.

IV. CONCLUSION

In this paper, we demonstrate the use of nanoconfined ferromagnetic-resonance modes in nanopatterned magnetic layers for sensing a wide range of magnetic-particle sizes. This demonstration is motivated by the potential for the development of frequency-based (rather than voltage-based) sensing methods for use in magnetic biosensing. Resonance-based particle detection is carried out for magnetic particles with sizes ranging from 6 nm to 4 μm. The particles' stray magnetic fields act directly on the precessing moments within the magnetic layers, generating significant shifts in the resonance fields (or, equivalently, the resonant frequencies). Thanks to this direct action, the observed resonance shifts in our hole-based patterned ferromagnet can be maintained over large ranges of fields, meaning that resonance-based nanoparticle detection can be used in the presence of strong magnetic fields, where particle moments (and thus particle-generated fields) can be maximized. Even in the macroscopic hole array studied here, the dominant effect of the particles is typically a resonance shift rather than a broadening of the resonance linewidth, a result which is encouraging for the future implementation of a sensing method based on sensitively detecting changes to resonance frequencies.

In this work, we also identify different characteristics in the resonance shifts for small and large particles. For small particles, their preferential capture in our system's nanoscale holes means that the majority of the particles act on the resonance modes in unison, generating clear, mode-dependent resonance shifts and mode-dependent shift polarities which persist to very high particle coverages. Shifts at intermediate and large particle coverages can be well reproduced via simulation for the 130 nm particles. In contrast to the case of small particles, however, the effect of microbeads is analogous to that seen in continuous films, with the two major resonance modes both shifting weakly in the same direction. This effect is due to a lack of particle localization with respect to the spatially periodic nanoscale regions where the modes are localized. Although suboptimal, detection is nevertheless achieved in such geometries, albeit with low resonance shifts which are similar to those observed in continuous films. Note that the ability to detect particles is determined not only by how sensitive the frequency is to changes in the magnetic field but also by the ability to generate clear modifications to these frequencies due to favorable particle positioning. A proper choice of particle size and reliable positioning of particles close to well-localized modes is thus a critical factor in resonance-based sensing.

ACKNOWLEDGMENTS

This research is supported by the Australian Research Council's Discovery Early Career Researcher Award scheme (Grant No. DE120100155) and Discovery Projects scheme (Grant No. DP110103980) and the U.S. Air Force [Asian Office of Aerospace Research and Development (AOARD)]. The University of Western Australia (UWA) also supported this research via the following programs: Research Development Award, Research Collaboration Award, Early Career Researcher Fellowship Support, Scholarship for International Research Fees, University Postgraduate Award (International Students), Re-Entry Fellowship, Teaching Relief and School of Physics Vacation Scholarship. This work is also supported by resources provided by the Pawsey Supercomputing Centre with funding from the Australian Government and the Government of Western Australia. A. O. A. is supported by the National Research Foundation, Prime Minister's Office, Singapore under its Competitive Research Programme (CRP Grant No. NRF-CRP 10-2012-03). The authors thank C. Lueng, M. Albert, W. Wang, A. Suvorova, A. Dodd, C. Yang, D. Schibeci, A. Chew, and R. C. Bording for their assistance. The authors acknowledge access to the UWA Biomagnetics Wet Laboratory and Magnetic Characterisation Facility and the facilities and the scientific and technical assistance of the Australian Microscopy & Microanalysis Research Facility at the Centre for Microscopy, Characterisation and Analysis, The University of Western Australia, a facility funded by the University, State, and Commonwealth Governments.

APPENDIX: ADDITIONAL MAGNETIC-PARTICLE DETAILS

The following particles are used for the sensing experiments. (i) (6 ± 1)-nm-wide iron-oxide nanoparticles (see below). (ii) nanomag-D(-spio) cluster-shaped particles (79-00-501 and 09-00-132; Micromod Partikeltechnologie GmbH) with stated diameters of 50 and 130 nm. (iii) 880-nm-wide magnetic beads (PMC1N; Bangs Laboratories, Inc.) consisting of iron-oxide nanoparticles within a polymer matrix. (iv) 4.14-μm beads (PM-40-10; SpheroTech, Inc.) consisting of a polystyrene core coated with a mixture of polystyrene and magnetic nanoparticles. Concentrations of commercial particle solutions (all aqueous) are determined from the manufacturer's specifications after dilution in purified water. The 6-nm iron-oxide nanoparticles are synthesized under standard Schlenk conditions using the methodology developed by Sun *et al.* [59]. Briefly, $Fe(acac)^3$ (0.7 g, 2 mmol) and 1,2-hexadecanediol (2.5 g, 10 mmol) are dissolved in benzyl ether (20 mL) containing oleylamine (6 mmol) and oleic acid (6 mmol). The resulting mixture is heated at 200 °C for 2 h, increased to 260 °C, held for 1 h, then cooled to room temperature. The particles are precipitated by the addition of ethanol (40 mL), centrifuged

(5000 rpm, 10 min), and redispersed in 1,2-dichlorobenzene to the required concentration. These particles have been fully characterized by a range of routine techniques (see Fig. 10 in the Supplemental Material [57]).

[1] D. R. Baselt, G. U. Lee, M. Natesan, S. W. Metzger, P. E. Sheehan, and R. J. Colton, A biosensor based on magnetoresistance technology, Biosens. Bioelectron. **13**, 731 (1998).

[2] R. S. Gaster, D. A. Hall, C. H. Nielsen, S. J. Osterfeld, H. Yu, K. E. Mach, R. J. Wilson, B. Murmann, J. C. Liao, S. S. Gambhir *et al.*, Matrix-insensitive protein assays push the limits of biosensors in medicine, Nat. Med. **15**, 1327 (2009).

[3] H. Lee, T.-H. Shin, J. Cheon, and R. Weissleder, Recent developments in magnetic diagnostic systems, Chem. Rev. **115**, 10690 (2015).

[4] E. Ng, K. C. Nadeau, and S. X. Wang, Giant magnetoresistive sensor array for sensitive and specific multiplexed food allergen detection, Biosens. Bioelectron. **80**, 359 (2016).

[5] Y. Li, B. Srinivasan, Y. Jing, X. Yao, M. A. Hugger, J.-P. Wang, and C. Xing, Nanomagnetic competition assay for low-abundance protein biomarker quantification in unprocessed human sera, J. Am. Chem. Soc. **132**, 4388 (2010).

[6] B. Srinivasan, Y. Li, Y. Jing, C. Xing, J. Slaton, and J.-P. Wang, A three-layer competition-based giant magnetoresistive assay for direct quantification of endoglin from human urine, Anal. Chem. **83**, 2996 (2011).

[7] C. Duarte, T. Costa, C. Carneiro, R. Soares, A. Jitariu, S. Cardoso, M. Piedade, R. Bexiga, and P. Freitas, Semiquantitative method for streptococci magnetic detection in raw milk, Biosensors **6**, 19 (2016).

[8] Y. R. Chemla, H. L. Grossman, Y. Poon, R. McDermott, R. Stevens, M. D. Alper, and J. Clarke, Ultrasensitive magnetic biosensor for homogeneous immunoassay, Proc. Natl. Acad. Sci. U.S.A. **97**, 14268 (2000).

[9] P.-A. Besse, G. Boero, M. Demierre, V. Pott, and R. Popovic, Detection of a single magnetic microbead using a miniaturized silicon Hall sensor, Appl. Phys. Lett. **80**, 4199 (2002).

[10] M. M. Miller, G. A. Prinz, S.-F. Cheng, and S. Bounnak, Detection of a micron-sized magnetic sphere using a ring-shaped anisotropic magnetoresistance-based sensor: A model for a magnetoresistance-based biosensor, Appl. Phys. Lett. **81**, 2211 (2002).

[11] L. Ejsing, M. F. Hansen, A. K. Menon, H. A. Ferreira, D. L. Graham, and P. P. Freitas, Magnetic microbead detection using the planar Hall effect, J. Magn. Magn. Mater. **293**, 677 (2005).

[12] P. I. Nikitin, P. M. Vetoshko, and T. I. Ksenevich, New type of biosensor based on magnetic nanoparticle detection, J. Magn. Magn. Mater. **311**, 445 (2007).

[13] M. Donolato, M. Gobbi, P. Vavassori, M. Leone, M. Cantoni, V. Metlushko, B. Ilic, M. Zhang, S. X. Wang, and R. Bertacco, Nanosized corners for trapping and detecting magnetic nanoparticles, Nanotechnology **20**, 385501 (2009).

[14] L. Di Michele, C. Shelly, P. de Marco, P. See, D. Cox, and O. Kazakova, Detection and susceptibility measurements of a single Dynal bead, J. Appl. Phys. **110**, 063916 (2011).

[15] S. M. Hira, K. Aledealat, K.-S. Chen, M. Field, G. J. Sullivan, P. B. Chase, P. Xiong, S. von Molnár, and G. F. Strouse, Detection of target ssDNA using a microfabricated Hall magnetometer with correlated optical readout, J. Biomed. Biotechnol. **2012**, 492730 (2012).

[16] J. Devkota, A. Ruiz, P. Mukherjee, H. Srikanth, and M.-H. Phan, Magneto-impedance biosensor with enhanced sensitivity for highly sensitive detection of nanomag-D beads, IEEE Trans. Magn. **49**, 4060 (2013).

[17] H. J. Chung, C. M. Castro, H. Im, H. Lee, and R. Weissleder, A magneto-DNA nanoparticle system for rapid detection and phenotyping of bacteria, Nat. Nanotechnol. **8**, 369 (2013).

[18] V. O. Shipunova, M. P. Nikitin, P. I. Nikitin, and S. M. Deyev, MPQ-cytometry: A magnetism-based method for quantification of nanoparticle-cell interactions, Nanoscale **8**, 12764 (2016).

[19] J. Llandro, T. J. Hayward, D. Morecroft, J. A. C. Bland, F. J. Castano, I. A. Colin, and C. A. Ross, Quantitative digital detection of magnetic beads using pseudo-spin-valve rings for multiplexed bioassays, Appl. Phys. Lett. **91**, 203904 (2007).

[20] B. Srinivasan, Y. Li, Y. Jing, Y. Xu, X. Yao, C. Xing, and J.-P. Wang, A detection system based on giant magnetoresistive sensors and high-moment magnetic nanoparticles demonstrates zeptomole sensitivity: Potential for personalized medicine, Angew. Chem., Int. Ed. Engl. **48**, 2764 (2009).

[21] S. J. Osterfeld, H. Yu, R. S. Gaster, S. Caramuta, L. Xu, S.-J. Han, D. A. Hall, R. J. Wilson, S. Sun, R. L. White *et al.*, Multiplex protein assays based on real-time magnetic nanotag sensing, Proc. Natl. Acad. Sci. U.S.A. **105**, 20637 (2008).

[22] D. Hall, R. Gaster, T. Lin, S. Osterfeld, S. Han, B. Murmann, and S. Wang, GMR biosensor arrays: A system perspective, Biosens. Bioelectron. **25**, 2051 (2010).

[23] P. P. Freitas, F. A. Cardoso, V. C. Martins, S. A. M. Martins, J. Loureiro, J. Amaral, R. C. Chaves, S. Cardoso, L. P. Fonseca, A. M. Sebastião *et al.*, Spintronic platforms for biomedical applications, Lab Chip **12**, 546 (2012).

[24] J.-R. Lee, N. Sato, D. J. B. Bechstein, S. J. Osterfeld, J. Wang, A. W. Gani, D. A. Hall, and S. X. Wang, Experimental and theoretical investigation of the precise transduction mechanism in giant magnetoresistive biosensors, Sci. Rep. **6**, 18692 (2016).

[25] D. Issadore, J. Chung, H. Shao, M. Liong, A. A. Ghazani, C. M. Castro, R. Weissleder, and H. Lee, Ultrasensitive clinical enumeration of rare cells ex vivo using a micro-Hall detector, Sci. Transl. Med. **4**, 141ra92 (2012).

[26] P. M. Braganca, B. A. Gurney, B. A. Wilson, J. A. Katine, S. Maat, and J. R. Childress, Nanoscale magnetic field detection using a spin torque oscillator, Nanotechnology **21**, 235202 (2010).

[27] R. J. Ryan, H. Xi, and I. Jin, Magnetic oscillator based biosensor, U.S. Patent No. US8053244 B2 (8 November 2011).

[28] M. Inoue, A. Baryshev, H. Takagi, P. B. Lim, K. Hatafuku, J. Noda, and K. Togo, Investigating the use of magnonic crystals as extremely sensitive magnetic field sensors at room temperature, Appl. Phys. Lett. **98**, 132511 (2011).

[29] J. P. Fried and P. J. Metaxas, Localized magnetic fields enhance the field sensitivity of the gyrotropic resonance frequency of a magnetic vortex, Phys. Rev. B **93**, 064422 (2016).

[30] P. J. Metaxas, M. Sushruth, R. Begley, J. Ding, R. C. Woodward, I. Maksymov, M. Albert, W. Wang, H. Fangohr, A. Adeyeye, and M. Kostylev, Sensing magnetic nanoparticles using nano-confined ferromagnetic resonances in a magnonic crystal, Appl. Phys. Lett. **106**, 232406 (2015).

[31] M. Albert, M. Beg, D. Chernyshenko, M.-A. Bisotti, R. L. Carey, H. Fangohr, and P. J. Metaxas, Frequency-based nanoparticle sensing over large field ranges using the ferromagnetic resonances of a magnetic nanodisc, arXiv: 1604.07277 [Nanotechnology (to be published)].

[32] K. Mizushima, K. Kudo, T. Nagasawa, and R. Sato, Signal-to-noise ratios in high-signal-transfer-rate read heads composed of spin-torque oscillators, J. Appl. Phys. **107**, 063904 (2010).

[33] J. R. Petrie, S. Urazhdin, K. A. Wieland, G. A. Fischer, and A. S. Edelstein, Using a spin torque nano-oscillator to read memory based on the magnetic permeability, J. Phys. D: Appl. Phys. **47**, 055002 (2014).

[34] I. N. Krivorotov, N. C. Emley, J. C. Sankey, S. I. Kiselev, D. C. Ralph, and R. A. Buhrman, Time-domain measurements of nanomagnet dynamics driven by spin-transfer torques, Science **307**, 228 (2005).

[35] H. Suto, T. Nagasawa, K. Kudo, K. Mizushima, and R. Sato, Real-time measurement of temporal response of a spin-torque oscillator to magnetic pulses, Appl. Phys. Express **4**, 013003 (2011).

[36] Z. Zeng, P. K. Amiri, I. N. Krivorotov, H. Zhao, G. Finocchio, J.-P. Wang, J. A. Katine, Y. Huai, J. Langer, K. Galatsis *et al.*, High-power coherent microwave emission from magnetic tunnel Junction nano-oscillators with perpendicular anisotropy, ACS Nano **6**, 6115 (2012).

[37] E. Grimaldi, A. Dussaux, P. Bortolotti, J. Grollier, G. Pillet, A. Fukushima, H. Kubota, K. Yakushiji, S. Yuasa, and V. Cros, Response to noise of a vortex based spin transfer nano-oscillator, Phys. Rev. B **89**, 104404 (2014).

[38] J. Loureiro, R. Ferreira, S. Cardoso, P. P. Freitas, J. Germano, C. Fermon, G. Arrias, M. Pannetier-Lecoeur, F. Rivadulla, and J. Rivas, Toward a magnetoresistive chip cytometer: Integrated detection of magnetic beads flowing at cm/s velocities in microfluidic channels, Appl. Phys. Lett. **95**, 034104 (2009).

[39] J. Loureiro, P. Z. Andrade, S. Cardoso, C. L. da Silva, J. M. Cabral, and P. P. Freitas, Spintronic chip cytometer, Appl. Phys. Lett. **109**, 07B311 (2011).

[40] M. Helou, M. Reisbeck, S. F. Tedde, L. Richter, L. Bär, J. J. Bosch, R. H. Stauber, E. Quandt, and O. Hayden, Time-of-flight magnetic flow cytometry in whole blood with integrated sample preparation, Lab Chip **13**, 1035 (2013).

[41] M. Krawczyk and D. Grundler, Review and prospects of magnonic crystals and devices with reprogrammable band structure, J. Phys. Condens. Matter **26**, 123202 (2014).

[42] J. Ding, M. Kostylev, and A. O. Adeyeye, Magnonic Crystal as a Medium with Tunable Disorder on a Periodical Lattice, Phys. Rev. Lett. **107**, 047205 (2011).

[43] B. Lenk, H. Ulrichs, F. Garbs, and M. Münzenberg, The building blocks of magnonics, Phys. Rep. **507**, 107 (2011).

[44] A. Manzin, G. Barrera, F. Celegato, M. Coïsson, and P. Tiberto, Influence of lattice defects on the ferromagnetic resonance behaviour of 2D magnonic crystals, Sci. Rep. **6**, 22004 (2016).

[45] H. P. Erickson, Size and shape of protein molecules at the nanometer level determined by sedimentation, gel filtration, and electron microscopy, Biol. Proced. Online **11**, 32 (2009).

[46] L. Li, K. Y. Mak, C. W. Leung, S. M. Ng, Z. Q. Lei, and P. W. T. Pong, Detection of 10-nm superparamagnetic iron oxide nanoparticles using exchange-biased GMR sensors in Wheatstone bridge, IEEE Trans. Magn. **49**, 4056 (2013).

[47] V. Pospichalova, J. Svoboda, Z. Dave, A. Kotrbova, K. Kaiser, D. Klemova, L. Ilkovics, A. Hampl, I. Crha, E. Jandakova, L. Minar, V. Weinberger, and V. Bryja, Simplified protocol for flow cytometry analysis of fluorescently labeled exosomes and microvesicles using dedicated flow cytometer, J. Extracell. Vesicles **4**, 25530 (2015).

[48] N. Singh, S. Goolaup, and A. O. Adeyeye, Fabrication of large area nanomagnets, Nanotechnology **15**, 1539 (2004).

[49] I. S. Maksymov and M. Kostylev, Broadband stripline ferromagnetic resonance spectroscopy of ferromagnetic films, multilayers and nanostructures, Physica (Amsterdam) **69E**, 253 (2015).

[50] E. N. Ivanov and M. Kostylev, Extremely high-resolution measurements of microwave magnetisation dynamics in magnetic thin films and nanostructures, arXiv:1402.3459.

[51] H. Fangohr, G. Bordignon, M. Franchin, A. Knittel, P. A. J. de Groot, and T. Fischbacher, A new approach to (quasi) periodic boundary conditions in micromagnetics: The macrogeometry, J. Appl. Phys. **105**, 07D529 (2009).

[52] A. Vansteenkiste, J. Leliaert, M. Dvornik, M. Helsen, F. Garcia-Sanchez, and B. Van Waeyenberg, The design and verification of MuMax3, AIP Adv. **4**, 107133 (2014).

[53] J. D. Hunter, MATPLOTLIB: A 2D graphics environment, IEEE Comput. Sci. Eng. **9**, 90 (2007).

[54] S. van der Walt, S. C. Colbert, and G. Varoquaux, The NumPy array: A structure for efficient numerical computation, IEEE Comput. Sci. Eng. **13**, 22 (2011).

[55] P. J. Metaxas, M. Albert, S. Lequeux, V. Cros, J. Grollier, P. Bortolotti, A. Anane, and H. Fangohr, Resonant translational, breathing, and twisting modes of transverse magnetic domain walls pinned at notches, Phys. Rev. B **93**, 054414 (2016).

[56] T. Fischbacher, M. Franchin, G. Bordignon, and H. Fangohr, A systematic approach to multiphysics extensions of finite-element-based micromagnetic simulations: NMAG, IEEE Trans. Magn. **43**, 2896 (2007).

[57] See Supplemental Material at http://link.aps.org/supplemental/10.1103/PhysRevApplied.6.044005 for additional scanning electron micrographs, experimental results and simulation results.

[58] J. Ding, N. Singh, M. Kostylev, and A. O. Adeyeye, Static and dynamic magnetic properties of $Ni_{80}Fe_{20}$ anti-ring nanostructures, Phys. Rev. B **88**, 014301 (2013).

[59] S. Sun, H. Zeng, D. B. Robinson, S. Raoux, P. M. Rice, S. X. Wang, and G. Li, Monodisperse MFe_2O_4 (M = Fe, Co, Mn) nanoparticles, J. Am. Chem. Soc. **126**, 273 (2004).